AIAA JOURNAL
Vol. 55, No. 7, July 2017

Wall-Modeled Large-Eddy Simulation of Autoignition-Dominated Supersonic Combustion

Graham V. Candler*
University of Minnesota, Minneapolis, Minnesota 55455
and
Niccolo Cymbalist† and Paul E. Dimotakis‡
California Institute of Technology, Pasadena, California 91125

DOI: 10.2514/1.J055550

Simulations of combustion in high-speed and supersonic flows need to account for autoignition phenomena, compressibility, and the effects of intense turbulence. In the present work, the evolution-variable manifold framework of Cymbalist and Dimotakis ("On Autoignition-Dominated Supersonic Combustion," AIAA Paper 2015-2315, June 2015) is implemented in a computational fluid dynamics method, and Reynolds-averaged Navier–Stokes and wall-modeled large-eddy simulations are performed for a hydrogen–air combustion test case. As implemented here, the evolution-variable manifold approach solves a scalar conservation equation for a reaction-evolution variable that represents both the induction and subsequent oxidation phases of combustion. The detailed thermochemical state of the reacting fluid is tabulated as a low-dimensional manifold as a function of density, energy, mixture fraction, and the evolution variable. A numerical flux function consistent with local thermodynamic processes is developed, and the approach for coupling the computational fluid dynamics to the evolution-variable manifold table is discussed. Wall-modeled large-eddy simulations incorporating the evolution-variable manifold framework are found to be in good agreement with full chemical kinetics model simulations and the jet in supersonic crossflow hydrogen–air experiments of Gamba and Mungal ("Ignition, Flame Structure and Near-Wall Burning in Transverse Hydrogen Jets in Supersonic Crossflow," *Journal of Fluid Mechanics*, Vol. 780, Oct. 2015, pp. 226–273). In particular, the evolution-variable manifold approach captures both thin reaction fronts and distributed reaction-zone combustion that dominate high-speed turbulent combustion flows.

Nomenclature

a	=	speed of sound, m/s
$\mathcal{C}, \mathcal{X}, \mathcal{Z}$	=	progress variable, nonfuel mass fraction, and fuel mass fraction
$c_v, c_{v,s}$	=	mixture and s-species specific heats, J/(kg · K)
D	=	diffusion coefficient, m^2/s
E	=	total energy per unit volume, J/m^3
e, e_s	=	mixture and s-species specific energy, J/kg
$\boldsymbol{F}$	=	convective flux vector
h, h_0	=	enthalpy and total enthalpy, J/kg
i	=	grid index
J	=	jet momentum ratio
$\boldsymbol{j}_h$	=	diffusive enthalpy flux
k	=	kinetic energy, J/kg
L, R	=	values obtained from left and right data
M_s	=	s-species molar mass, kg/kmol
N_s	=	number of species in detailed kinetics model
$\hat{\boldsymbol{n}}, n_x, n_y, n_z$	=	element face unit normal vector and components
p	=	pressure, Pa
q_j	=	heat flux vector
R, R^{-1}	=	eigenvector matrices
$\hat{R}$	=	universal (molar) gas constant, J/(kmol · K)
$\bar{R}$	=	mixture (specific) gas constant, J/(kg · K)
s	=	species index
T	=	temperature, K
t	=	time, s
U, V	=	vectors of conserved and primitive variables
$\boldsymbol{u}; u, v, w$	=	velocity vector and components, m/s
u'	=	face-normal velocity component, m/s
$\boldsymbol{x}, x_j$	=	position vector and its components, m
Y_s	=	s-species mass fraction
α	=	dissipative flux factor
δ_R	=	reaction-zone thickness, m
ε	=	dissipation rate
ζ	=	evolution-variable source term, 1/s
η_k	=	Kolmogorov length scale, m
Λ, λ	=	diagonal matrix of eigenvalues and eigenvalue
ν_t, ν	=	turbulence field variable and kinematic viscosity
ρ, ρ_s	=	density and s-species density, kg/m^3
σ_{ij}	=	viscous and Reynolds stress
τ	=	evolution variable
ϕ	=	stoichiometric fuel–air ratio
χ	=	subgrid-scale relaxation-rate parameter
$\dot{\omega}_s$	=	s-species chemical source term, 1/s
$\pm$	=	flux directions

Subscript

eq	=	equilibrium state

Presented as Paper 2015-3340 at the 45th AIAA Fluid Dynamics Conference, Dallas, TX, 22–25 June 2015; received 28 July 2016; revision received 15 December 2016; accepted for publication 3 January 2017; published online 13 April 2017.

*Russell J. Penrose and McKnight Presidential Professor, Aerospace Engineering and Mechanics. Fellow AIAA.
†Associate, Thermal Sciences, Exponent. 5401 McConnell Ave., Los Angeles CA 90066.
‡John K. Northrop Professor of Aeronautics and Professor of Applied Physics. Fellow AIAA.

I. Introduction

RELIABLE simulation of turbulent combustion in high-speed airbreathing engines is important for their design and optimization. The most promising approach for representing these complex flows is large-eddy simulation (LES), in which large-scale turbulent motion is resolved and small-scale effects are modeled. There are several widely used approaches for the LES of combustion, but most were originally developed for combustion in low-speed flows and in combustion regimes that can be approximated as a collection of thin flamelets [1,2]. In high-speed flows, several effects

become important: compressibility that is coupled to heat release, ignition delay, and combustion in a distributed reaction-zone (DRZ) regime.

To illustrate these effects, consider a convected fluid element undergoing combustion. First, the fuel gradually decomposes into radicals; then, ignition occurs, followed by rapid oxidation and heat release. With high convection speeds, the initial decomposition step and ignition delay may span a large physical distance in the combustor, and dominate overall engine performance. For example, a 1 ms ignition delay in a flow traveling at 1000 m/s results in a 1 m induction length. The notional convected fluid element also undergoes mixing with the surrounding fluid, resulting in a partially premixed state. The intense turbulence generated by the high-speed flow yields Kolmogorov length scales of a few micrometers. Thus, the Kolmogorov-scale eddies are approximately an order of magnitude smaller than the typical reaction-zone thickness of a flame, and they are expected to penetrate reaction zones and break down local flamelet structures into locally distributed reactions (e.g., Law [3]). This is supported by direct numerical simulation results by Aspden et al. [4] and subsequently experimentally confirmed by Zhou et al. [5]. This combustion regime occurs in the near-wall burning of a fuel jet in a supersonic crossflow: for example, as in [6] and as will be demonstrated with a posteriori analysis of the current simulations. Thus, the goal of the current work is to develop a combustion modeling approach for the LES of high-speed combustion flows that can capture both ignition-delay and DRZ combustion effects.

There have been many reviews of turbulent combustion modeling approaches for the LES of high-speed flows. Fureby [7], Foster and Miller [8], Oefelein [9], and Gonzalez-Juez et al. [10] provide recent comprehensive surveys of the most widely used approaches. These include the family of flamelet and flamelet/progress variable (FPV) approaches, the linear eddy model (LEM), and transported probability density function (TPDF), and filtered mass density function (FMDF) methods. Each approach has its own set of physical assumptions and limitations, resulting in varying levels of fidelity and simulation costs.

The FPV approach [11] and many other related methods [12] assume that the combustion process occurs on a low-dimensional manifold that can be derived from one-dimensional flames. The manifold is precomputed and provides the thermochemical state during a simulation, assuming a probability density function for subgrid-scale (SGS) interactions between turbulence and combustion.

The LEM [13] approach is based on a one-dimensional stochastic representation of turbulent mixing within each grid element. It is often used in conjunction with approaches to reduce the cost of evaluating the chemical source term, such as in situ adaptive tabulation (ISAT) [14].

TPDF [15] and FMDF [16] methods are related, in that they solve transport equations for the probability density functions. Typically, these methods represent the statistics of the thermochemical state with an ensemble of Monte Carlo particles for which the transport is governed by a stochastic difference equation. An important advantage of the FMDF approach is that the chemical source term has a closed form.

These methods have been used for the LES of supersonic combustion flows. Recent examples include compressible FPV simulations by Chan and Ihme [17], Saghafian et al. [18], Wang et al. [19], and Cao et al. [20]; LEM simulations by Génin and Menon [21]; and TPDF and FMDF simulations by Delarue and Pope [22], Cocks et al. [23], and Irannejad et al. [24].

Recently, Cymbalist and Dimotakis [25,26] proposed an approach to model high-speed combustion flows, including the effects of ignition delay and combustion in the DRZ regime. Their evolution-variable manifold (EVM) approach explicitly represents ignition delay and subsequent heat release as separate phases of combustion. Combustion is represented by a well-stirred reactor that is given an initial condition and is integrated in time until it reaches equilibrium. The time domain is then converted to the evolution variable τ that tracks the variation of the gas state from the initial condition ($\tau = 0$) as it evolves to equilibrium ($\tau = 1$). In the flow simulation, τ is computed as a field variable, and its value represents the Lagrangian evolution of a fluid element as it flows through the computational domain. The EVM approach precomputes and tabulates the gas state as a low-dimensional manifold in terms of energy, density, mixture fraction, and evolution variable. A well-stirred reactor model is expected to represent the small-scale structure of DRZ combustion and is used to generate the manifold. With this approach, the complete thermodynamic state of the gas is accessible to the flowfield computation, making it possible to develop a numerical method that conserves energy and is consistent with the evolving thermochemical state. Because the manifold that describes the combustion process is precomputed, the EVM approach significantly reduces the simulation cost relative to full kinetics models, and even to ISAT-based methods. Thus, the EVM approach has the potential to greatly reduce the cost and improve the accuracy of large-eddy simulations of high-speed combustion flows.

Reliable simulation of high-speed turbulent combustion flows requires four modeling elements: compressible flow, near-wall turbulent motion, free or detached turbulent motion, and combustion including ignition-delay effects. In the present work, we use standard approaches for the first three elements, and we focus on the accurate and efficient modeling of turbulent combustion at conditions relevant to high-speed flight. To this end, we modify an existing computational fluid dynamics code [27] for the wall-modeled LES of compressible reacting flows to represent the detailed thermochemical state of the reacting fuel–air mixture. The focus is on the development of a numerical method that is rigorously consistent with the thermochemical model so that the numerical method correctly reflects the variations in the thermodynamic state. We apply the proposed numerical flux function to the supersonic reacting hydrogen injection experiments of Gamba and Mungal [6] using the hydrogen–air chemical kinetics model of Burke et al. [28].

II. Evolution-Variable Manifold Approach

In this section, the evolution-variable manifold approach is briefly discussed. Additional details may be found in the work of Cymbalist and Dimotakis [25,26]. In the EVM framework, the state of a reacting gas is represented in terms of four flowfield variables. These are the thermodynamic state $[e, \rho]$, the fuel mixture fraction [2], $\mathcal{Z}$, and a reaction-evolution variable τ. Although the thermodynamic quantities and mixture fraction are conserved scalar quantities, the evolution variable has a source term ζ for which the value can be determined based on ignition-delay behavior before ignition and detailed chemical kinetics after ignition, as discussed in the following. The detailed state of the fluid is precomputed and stored in a four-dimensional table (manifold), spanning the thermodynamic state space of the reacting flow in question. At the LES runtime, the table is used by the computational fluid dynamics (CFD) code to provide the detailed state of the reacting flow.

For high-speed combustion flows, we assume that Lagrangian fluid elements in the DRZ regime can be modeled as well-stirred reactors (WSRs) convected by the flow. These convected fluid elements can be characterized by their thermodynamic state, stoichiometry (or mixture fraction), and extent of reaction evolution. We determine the detailed state of the fluid as a function of these variables using WSRs with constant mass, energy, and stoichiometry:

$$\frac{\mathrm{d}\rho}{\mathrm{d}t} = 0 \tag{1a}$$

where t is the reactor time, and

$$\frac{\mathrm{d}e}{\mathrm{d}t} = 0 \tag{1b}$$

Species within the WSR react with mass-fraction evolution equations given by

$$\frac{\mathrm{d}Y_s}{\mathrm{d}t} = \dot{\omega}_s(Y_1, Y_2, \ldots, Y_s, \ldots; e, \rho) + \chi(Y_{s,\mathrm{eq}} - Y_s), \quad s = 1, 2, \ldots, N_s \tag{1c}$$

where the Y_s are the s-species mass fractions, $\dot{\omega}_s$ is the species' chemical-production rate, and N_s is the total number of reacting species in the WSR. The role of χ is discussed in the following. These WSRs are initialized across the range of thermodynamic state and stoichiometry anticipated in the flow and run to equilibrium. The results are converted from the time domain to the evolution-variable domain as follows.

We can define a product mass fraction and its equilibrium value in the WSR as

$$\mathcal{C} = \sum_{s=\mathrm{prod}} Y_s, \quad \mathcal{C}_{\mathrm{eq}} = \sum_{s=\mathrm{prod}} Y_{s,\mathrm{eq}} \tag{2}$$

where the "eq" subscript indicates that the mass fraction is evaluated at the local thermodynamic equilibrium state. The evolution variable τ is defined as the ratio of the product mass fraction to its value at equilibrium, and its rate of change is denoted by ζ; these have the form

$$\tau = \frac{\mathcal{C}}{\mathcal{C}_{\mathrm{eq}}}, \quad \zeta = \frac{\dot{\omega}}{\mathcal{C}_{\mathrm{eq}}} = \frac{\sum_{\mathrm{prod}} \dot{\omega}_s}{\mathcal{C}_{\mathrm{eq}}} \tag{3}$$

Thus, τ tracks how far product formation has progressed relative to its final equilibrium condition. A similar definition of the progress variable in the FPV context was used by Cao et al. [20].

The relaxation parameter χ provides a simple model for SGS processes that promote the evolution of the gas mixture toward equilibrium, especially where the chemical reactions are slow. In the simulations presented in this paper, it is set to a constant value: $\chi = 10^4/\mathrm{s}$. Appendix A examines the effect of χ on the evolution rate of the WSR; it is shown that, under robust combustion conditions, χ has little effect; whereas at low-density conditions, it has the intended effect of increasing the rate of product formation to represent the subgrid-scale processes that drive the system toward equilibrium.

These equations provide the rate of change of the thermodynamic and chemical state of a fluid element undergoing combustion. A question then follows: How can constant-energy, -density, and -stoichiometry WSRs capture the behavior of convected reacting fluid elements, for which the energy, density, and stoichiometry may be changing as they progress from unburned to burned? The answer to that question lies in the assumption of path independence, i.e., that the state of the reacting fluid at some location in $[e, \rho, Z, \tau]$ space does not depend on the path (in state space) the fluid has taken to that location. For the hydrogen–air chemical-kinetic system in the present simulations, the solution to the convected WSR equations is found to be approximately independent of the reaction trajectory taken through the state space $[e, \rho, \mathcal{Z}]$; see Appendix B for details. This trajectory independence can be illustrated by considering two WSRs that are initialized with different values of $[e, \rho, \mathcal{Z}]$ and integrated in time (corresponding to τ). If the two reactors happen to pass through the same point in $[e, \rho, \mathcal{Z}, \tau]$ space and their thermochemical state at that point is found to be close to one another, then their state is trajectory independent. Appendix B shows that, for the hydrogen–air system studied here, the approximation of trajectory independence is very good for lean and near-stoichiometric WSRs, and it is valid within 10% for rich conditions. This approximation greatly simplifies the population of the EVM manifold because the WSRs may be integrated on constant-$[e, \rho, \mathcal{Z}]$ trajectories.

Before ignition, the evolution variable τ is defined by the extent of the WSR's progress toward ignition. For the hydrogen–air system, this phase of the reaction is reliably predicted by detailed chemical kinetics and requires no special handling. However, when the induction period is poorly predicted by detailed chemical kinetics, the EVM methodology offers an alternative data-driven approach incorporating a characteristic ignition-delay time, and it has been applied to ethylene [25,26]. A similar approach was used by Li et al. [29] to represent the induction process in the simulation of detonations. Postignition, τ is defined as the ratio of the total combustion product mass fraction to its local equilibrium mass fraction, and its source term ζ is given by the chemical source term of combustion products [Eq. (3)]. This approach has the potential to be extended to recent lumped-reduced reaction models for longer-chain hydrocarbons, in which fuel cracking is treated as an initial step before oxidation [30].

Solution trajectories in the state space of the WSR equations are used to populate a table of the chemical state of the gas mixture and ζ as a function of all values of $[e, \rho, \mathcal{Z}]$ and τ encountered in the flow regions of interest. Once the table has been constructed, the partial derivatives of ζ with respect to the table coordinates are also computed and tabulated for use in the implicit numerical method. Thus, during a flow simulation at any given grid element, the local values of $[e, \rho, \mathcal{Z}, \tau]$ are used to determine the corresponding values of Y_s, ζ, and the ζ derivatives by interpolation on the table. Then, all additional thermodynamic variables, such as pressure, temperature, speed of sound, gas constant, and specific heats, are constructed from the local density and energy and the tabulated mass fractions. Here, we use the McBride and Gordon thermodynamic curve fits [31] for the thermodynamics computations.

Figure 1 plots ζ and the water (H_2O) mass fraction as a function of $[\rho, \mathcal{Z}, \tau]$ at fixed e for the EVM table constructed to represent the hydrogen–air experiments of Gamba and Mungal [6]. The detailed chemical kinetics model of Burke et al. [28] was used to construct the table.

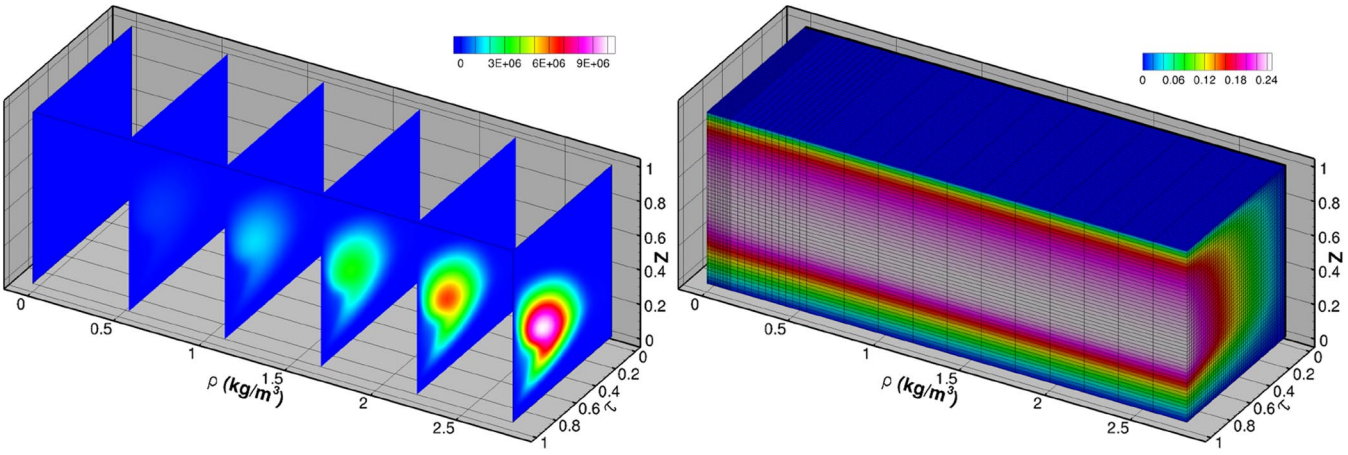

Fig. 1 Portion of the EVM table for the Gamba and Mungal experiment [6] at a constant value of energy ($e = 0.30$ MJ/kg): ζ (left) and mass fraction of H_2O (right).

III. EVM–LES Implementation

In this section, we discuss the integration of the EVM state tabulation with the wall-modeled LES. We focus on how the thermodynamic state and transport properties of the gas mixture are computed, which variables are tabulated, and how the diffusive enthalpy transport term is evaluated.

First, consider the calculation of the mixture state. Rather than tabulating all possible thermodynamic variables and transport properties (e.g., Saghafian et al. [18] in the context of a compressible FPV model), we follow the approach suggested by Oevermann [32] and used by Wang et al. [19]. That is, we tabulate the mass fractions obtained from the detailed chemistry WSR model and compute the local thermodynamic state from the density and energy computed by the CFD and the mass fractions interpolated from the table. This requires the use of thermodynamic data for the chemical species, such as the McBride–Gordon enthalpy curve fits [31]. Then, we can compute the mixture transport properties from the thermodynamic state and tabulated mass fractions.

One additional term requires attention. In the energy conservation equation [Eq. (6e)], the diffusive enthalpy flux

$$\boldsymbol{j}_h = \rho \sum_s Y_s v_{sj} h_s = -\rho D \sum_s h_s \frac{\partial Y_s}{\partial x_j} \tag{4}$$

involves the computation of the species enthalpy and gradients of the detailed model mass fractions (assuming Fickian diffusion). Quinlan et al. [33] proposed a simplification to this term of the following form:

$$\boldsymbol{j}_h \cong -\rho D \sum_s h_s \frac{\partial Y_s}{\partial \mathcal{Z}} \frac{\partial \mathcal{Z}}{\partial x_j} \tag{5}$$

when this approximation is adequate, only the term

$$\sum_s h_s \frac{\partial Y_s}{\partial \mathcal{Z}}$$

must be tabulated. Their a priori analysis showed relatively minor differences using this approach compared to the full expression [33]. In our simulations, however, we found that this approximation is not sufficiently accurate, resulting in spurious temperature variations and poor numerical stability. Thus, in the work presented here, we use the full expression [Eq. (4)]. This requires storage of the values of Y_s at element centroids and the computation of Y_s gradients.

Also note that we solve for $\mathcal{C}$, which is the product mass fraction, but tabulate the product state with $\tau = \mathcal{C}/\mathcal{C}_{\text{eq}}$. However, $\mathcal{C}_{\text{eq}}$ is a function of $[e, \rho, \mathcal{Z}]$ only, and it can be obtained from the table by extracting the product mass fractions at $[e, \rho, \mathcal{Z}, \tau = 1]$. The local value of τ is then computed from Eq. (3) and used to obtain the local mixture state.

The EVM table is four-dimensional, and a general search in this domain would be expensive. However, it is stored as an ordered array, and the relationship between the values of the variables $[e, \rho, \mathcal{Z}, \tau]$ and their indices are known a priori. Thus, integer math can be used to determine the bounding indices of the location in the table, and then a tetralinear interpolation is performed to obtain the values of Y_s, ζ, and the ζ derivatives with respect to the tabulation variables. The table is stored as single-precision (32 bit) real values to reduce its size; we have verified that there are no detectable differences in the simulations with 32 and 64 bit precision.

To summarize, the LES provides the value of $[e, \rho, \mathcal{Z}, \tau]$ at each time step to the EVM table; the table then returns the detailed fluid composition vector $[Y_1, Y_2, \ldots, Y_s, \ldots]^{\text{T}}$ and product evolution rate, ζ, and its partial derivatives from the precomputed Lagrangian well-stirred reactor and ignition-delay model. Figure 2 illustrates the exchange of information between the LES and EVM modules during runtime.

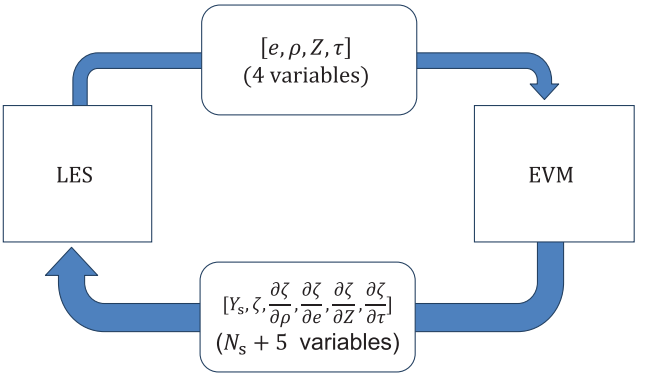

Fig. 2 Exchange of information between the LES and EVM modules during runtime.

IV. Governing Equations

In this section, we discuss the governing equations used for the EVM approach. As discussed previously, the detailed thermochemical state of the reacting fluid is determined at runtime from $[e, \rho, \mathcal{Z}, \tau]$. Note that τ is not a conserved variable, and we solve for the progress variable mass fraction $\mathcal{C}$ [Eq. (2)]. Thus, the compressible CFD code must solve conservation equations for the total density ρ, mixture fraction density $\rho\mathcal{Z}$, reaction product density $\rho\mathcal{C}$, momentum $\rho\boldsymbol{u}$, total energy $E = \rho(e + (1/2)\boldsymbol{u}\cdot\boldsymbol{u})$, and a turbulence field variable $\rho\nu_t$. These equations are as follows:

$$\frac{\partial \rho}{\partial t} + \frac{\partial}{\partial x_j}[\rho u_j] = 0 \tag{6a}$$

$$\frac{\partial \rho\mathcal{Z}}{\partial t} + \frac{\partial}{\partial x_j}[\rho\mathcal{Z}(u_j + v_{\mathcal{Z}j})] = 0 \tag{6b}$$

$$\frac{\partial \rho\mathcal{C}}{\partial t} + \frac{\partial}{\partial x_j}[\rho\mathcal{C}(u_j + v_{\mathcal{C}j})] = \rho\dot{\omega}_{\mathcal{C}} \tag{6c}$$

$$\frac{\partial \rho u_i}{\partial t} + \frac{\partial}{\partial x_j}[\rho u_i u_j + p\delta_{ij} - \sigma_{ij}] = 0 \tag{6d}$$

$$\frac{\partial E}{\partial t} + \frac{\partial}{\partial x_j}[(E + p)u_j - \sigma_{ij}u_i + q_j + \rho\sum_s Y_s v_{sj} h_s] = 0 \tag{6e}$$

$$\frac{\partial \rho\nu_t}{\partial t} + \frac{\partial}{\partial x_j}\left[\rho u_j \nu_t - \frac{1}{\sigma}\mu\frac{\partial \nu_t}{\partial x_j} - \frac{1}{\sigma}\sqrt{\rho}\nu_t\frac{\partial \sqrt{\rho}\nu_t}{\partial x_j}\right] = c_{b1}\hat{S}\rho\nu_t - c_{w1}f_w\rho\frac{\nu_t^2}{d^2} + c_{b2}\frac{\partial\sqrt{\rho}\nu_t}{\partial x_i}\frac{\partial\sqrt{\rho}\nu_t}{\partial x_i} \tag{6f}$$

Here, $v_{\mathcal{Z}j}$ and $v_{\mathcal{C}j}$ are the molecular and turbulent transport mass-diffusion velocities. The source term in the $\rho\mathcal{C}$ equation represents the progress variable production rate $\dot{\omega}_{\mathcal{C}} = \mathcal{C}_{\text{eq}}\zeta$, where ζ is the source term of the evolution variable, as described previously. The stress σ_{ij} includes the viscous stress and the Boussinesq approximation for the turbulent Reynolds stress. Likewise, the heat flux q_j includes molecular and turbulent transport. The equation for the turbulence field variable ν_t has the form taken from Catris and Aupoix [34] with turbulence modeling constants from the original Spalart and Allmaras paper [35]. See also the NASA Langley Turbulence Modeling Resource [36] for full details and for the form and values of the turbulence model parameters: $[\sigma, \hat{S}, c_{b1}, c_{b2}, c_{w1}, f_w]$. For the purposes of the wall-modeled LES discussed here, the improved delayed detached-eddy simulation (IDDES) approach of Shur et al. [37] is used to modify the source term of the turbulence transport equation to reduce dissipation away from walls; this results in a Smagorinsky-like SGS model [38] in regions of free or detached turbulent motion. Thus, the near-wall Reynolds-averaged Navier–Stokes (RANS) turbulence model provides surface shear and heat flux boundary conditions for the outer large-eddy simulation. This type of wall-modeled LES is a well-developed approach and has been used for many high-speed turbulent flow simulations.

In the preceding, $\rho\mathcal{Z}$ is the density of species comprising the fuel and its reaction products. We can define a complementary partial

density of the gas mixture as $\rho\mathcal{X} = \rho - \rho\mathcal{Z}$, which is the density of the gas mixture that is not composed of fuel and its reaction products. The conservation equation for $\rho\mathcal{X}$ is

$$\frac{\partial \rho\mathcal{X}}{\partial t} + \frac{\partial}{\partial x_j}[\rho\mathcal{X}(u_j + v_{\mathcal{X}j})] = 0 \tag{7}$$

with $v_{\mathcal{X}j} = -v_{\mathcal{Z}j}$ for mass conservation. In the following, we use the $\rho\mathcal{X}$ variable because it simplifies the derivation of the flux Jacobian and the formulation of the numerical flux function. Also, the resulting flux Jacobian has a form similar to that obtained for a mixture of reacting gases [39].

Thus, the vector of conserved quantities and the corresponding convective-flux vector for a three-dimensional flow are

$$U = [\rho\mathcal{X}, \rho\mathcal{Z}, \rho\mathcal{C}, \rho\boldsymbol{u}, E, \rho\nu_t]^{\mathrm{T}} \tag{8}$$

$$\boldsymbol{F} = [\rho\mathcal{X}u', \rho\mathcal{Z}u', \rho\mathcal{C}u', \rho\boldsymbol{u}u' + p\hat{\boldsymbol{n}}, (E+p)u', \rho\nu_t u']^{\mathrm{T}} \tag{9}$$

where $u' = \boldsymbol{u}\cdot\hat{\boldsymbol{n}}$ is the velocity normal to a cell face with unit normal vector $\hat{\boldsymbol{n}}$.

V. Numerical Method

In this section, we develop a numerical flux function for the coupled LES–EVM framework that uses the tabulated thermodynamic data. First, we develop the convective flux Jacobian required for an upwind-biased flux; then, we discuss an approach for obtaining second-order accurate fluxes, and finally provide a brief description of a low-dissipation higher-order centered flux function suitable for the LES of compressible flows.

A. Upwind Numerical Flux Formulation

Let us first consider an upwind flux formulation such as modified Steger–Warming flux vector splitting [40] or Roe flux-difference splitting [41]. Such a numerical flux is appropriate for RANS simulations of high-speed combustion flows. For LES applications, we use the dissipative portion of the upwind flux to stabilize a low-dissipation centered flux.

For the upwind flux, we must diagonalize the flux Jacobian: $\partial\boldsymbol{F}/\partial U$. This is straightforward, except for the derivatives of the pressure with respect to the conserved variables. Following the approach of Candler et al. [39], it can be shown that

$$\frac{\partial \boldsymbol{F}}{\partial U} = R^{-1}\Lambda R = \begin{pmatrix} \mathcal{X}\hat{\lambda}/a^2 \\ \mathcal{Z}\hat{\lambda}/a^2 \\ \mathcal{C}\hat{\lambda}/a^2 \\ (\boldsymbol{u}\hat{\lambda} + a\hat{\boldsymbol{n}}\tilde{\lambda})/a^2 \\ (h_o\hat{\lambda} + au'\tilde{\lambda})/a^2 \\ \nu_t\hat{\lambda}/a^2 \end{pmatrix} (p_{\rho\mathcal{X}} \;\; p_{\rho\mathcal{Z}} \;\; 0 \;\; -\boldsymbol{u}p_E \;\; p_E \;\; 0)$$

$$+ \begin{pmatrix} \mathcal{X}\tilde{\lambda}/a \\ \mathcal{Z}\tilde{\lambda}/a \\ \mathcal{C}\tilde{\lambda}/a \\ \boldsymbol{u}\tilde{\lambda}/a + \hat{\boldsymbol{n}}\hat{\lambda} \\ h_o\tilde{\lambda}/a + u'\hat{\lambda} \\ \nu_t\tilde{\lambda}/a \end{pmatrix} (-u' \;\; -u' \;\; 0 \;\; \hat{\boldsymbol{n}} \;\; 0 \;\; 0) + \lambda I \tag{10}$$

Where the diagonal matrix of eigenvalues is given as

$$\Lambda = \mathrm{diag}(\lambda, \lambda, \lambda, \lambda^+, \lambda, \lambda, \lambda^-, \lambda) \tag{11}$$

where $\lambda = u'$, $\lambda^+ = u' + a$, $\lambda^- = u' - a$, a is the speed of sound, $\tilde{\lambda}$ and $\hat{\lambda}$ are defined as

$$\tilde{\lambda} = \frac{1}{2}(\lambda^+ - \lambda^-) \quad \text{and} \quad \hat{\lambda} = \frac{1}{2}(\lambda^+ + \lambda^- - 2\lambda) \tag{12}$$

and $h_0 = e + p/\rho + (1/2)\boldsymbol{u}\cdot\boldsymbol{u}$ is the total enthalpy of the gas mixture.

The pressure derivatives

$$p_{\rho\mathcal{X}} = \frac{\partial p}{\partial \rho\mathcal{X}}, \quad p_{\rho\mathcal{Z}} = \frac{\partial p}{\partial \rho\mathcal{Z}}, \quad p_E = \frac{\partial p}{\partial E} \tag{13}$$

must be computed holding the conserved variables U fixed. For a multispecies mixture of thermally perfect gases, the pressure may be written as

$$p = \rho\sum_s Y_s \frac{\hat{R}}{M_s}T \tag{14}$$

To calculate the pressure derivatives, we can use the EVM table and the chain rule of differentiation to obtain the full expression for these quantities. For example,

$$\frac{\partial p}{\partial \rho\mathcal{X}} = \sum_s Y_s \frac{\hat{R}}{M_s}T + \rho\sum_s \frac{\partial Y_s}{\partial \rho\mathcal{X}}\frac{\hat{R}}{M_s}T + \rho\sum_s Y_s \frac{\hat{R}}{M_s}\frac{\partial T}{\partial \rho\mathcal{X}} \tag{15}$$

where these derivatives are taken holding $[\rho\mathcal{Z}, \rho\mathcal{C}, \rho\boldsymbol{u}, E, \rho\nu_t]$ fixed, and the Y_s derivatives are evaluated with finite differences on the EVM table. A simpler approach is to assume that Y_s is frozen during the differentiation, resulting in the closed-form expressions

$$\left.\frac{\partial p}{\partial \rho\mathcal{X}}\right|_{\rho\mathcal{Z},\rho\mathcal{C},\rho\boldsymbol{u},E,\rho\nu_t} = \left.\frac{\partial p}{\partial \rho\mathcal{Z}}\right|_{\rho\mathcal{X},\rho\mathcal{C},\rho\boldsymbol{u},E,\rho\nu_t} = \bar{R}T + \frac{\bar{R}}{c_v}\left(-e + \frac{1}{2}\boldsymbol{u}\cdot\boldsymbol{u}\right) \tag{16a}$$

$$\left.\frac{\partial p}{\partial E}\right|_{\rho\mathcal{Z},\rho\mathcal{X},\rho\mathcal{C},\rho\boldsymbol{u},\rho\nu_t} = \frac{\bar{R}}{c_v} \tag{16b}$$

where e, $\bar{R}$, and c_v are the mixture internal energy per unit mass, gas constant, and specific heat:

$$e = \sum_s Y_s e_s, \quad \bar{R} = \sum_s Y_s \frac{\hat{R}}{M_s}, \quad c_v = \sum_s Y_s c_{vs} \tag{17}$$

We implemented both approaches and found negligible differences, and therefore the simpler closed-form expressions are used. (This finding makes sense because the correct value of pressure is obtained when the frozen Y_s approximation is made.)

The preceding equations provide a complete expression for the convective flux Jacobian, which can be used to formulate an upwind numerical flux function. For example, the Roe flux is [41]

$$\boldsymbol{F}_{i+1/2} = \frac{1}{2}(\boldsymbol{F}_i + \boldsymbol{F}_{i+1}) - \frac{1}{2}\tilde{R}^{-1}|\tilde{\Lambda}|\tilde{R}(U_{i+1} - U_i) \tag{18}$$

where the tilde variables are Roe averaged using left and right data. For modified Steger–Warming flux vector splitting [40], the convective fluxes may be written as follows:

$$\boldsymbol{F}_{i+1/2} = (R^{-1}\Lambda^+ R)_{i+1/2}U^L + (R^{-1}\Lambda^- R)_{i+1/2}U^R \tag{19}$$

where $\Lambda^{\pm}$ are the positive and negative eigenvalue matrices.

The quantities $U^{L,R}$ are the conserved variables evaluated at the face using left- and right-biased data. For highly compressible flows, it is more robust and accurate to evaluate the primitive variables at the face and reconstruct the face values of the conserved variables [39]. Thus, with MUSCL-type limiting [42], we have

$$V^L_{i+1/2} = V_i + \frac{1}{2}\lim(V_{i+1} - V_i, V_i - V_{i-1}) \tag{20a}$$

$$V^R_{i+1/2} = V_{i+1} - \frac{1}{2}\lim(V_{i+2} - V_{i+1}, V_{i+1} - V_i) \tag{20b}$$

where

$$V = (\rho\mathcal{X}, \rho\mathcal{Z}, \rho\mathcal{C}, \boldsymbol{u}, v, w, p, \rho\nu_t)^{\mathrm{T}}$$

All conserved variables can then be obtained from the primitives, except for $E^{L,R}$.

We find that the solution is sensitive to how the energy at the face $E^{L,R}$ is reconstructed. The most accurate approach is to store the mass fractions Y_s obtained from the table for every grid element. Then, these mass fractions are limited as in Eq. (20), and are used to form the mixture-averaged gas constant at the face $\bar{R}^{L,R}$. The face temperature is then obtained from the face values of density and pressure:

$$T^{L,R} = \frac{p^{L,R}}{\rho^{L,R}\bar{R}^{L,R}} \tag{21}$$

Now, the face thermodynamic state is uniquely specified, and $E^{L,R}$ can be computed from $Y_s^{L,R}$ and $T^{L,R}$. This is the approach used in the present work.

Other less-accurate energy reconstruction approaches were tested with poor results. These methods included assuming that the gas state was frozen between the upwind element centroid and the face, and reconstructing the internal energy using a Taylor series for the energy and its derivatives. These approaches resulted in spurious nonmonotone temperature variations across reaction fronts, and the implicit time integration was less stable. Thus, we concluded that the complete energy reconstruction was required.

B. Kinetic Energy Consistent Flux

The wall-modeled LES results presented in the following were computed with a fourth-order-accurate centered flux function that has low levels of numerical dissipation. The flux is formulated so that it is discretely consistent with the compressible kinetic energy equation [43]. The dissipative component of the modified Steger–Warming flux discussed previously is added to provide dissipation near shock waves and other strong gradients. The Ducros et al. [44] sensor is used to activate the dissipative flux through a weight function α. The kinetic energy consistent (KEC) numerical flux may be written as

$$\boldsymbol{F}_{i+1/2} = \boldsymbol{F}_{\mathrm{KEC},i+1/2} - \alpha\frac{1}{2}(R^{-1}|\Lambda|R)_{i+1/2}(U_{i+1} - U_i) \tag{22}$$

and the sensor is given by

$$\alpha = \frac{(\nabla\cdot\boldsymbol{u})^2}{(\nabla\cdot\boldsymbol{u})^2 + (\nabla\times\boldsymbol{u})^2 + \epsilon} \tag{23}$$

with ϵ as a small positive number to prevent division by zero. The centered flux is

$$\boldsymbol{F}_{\mathrm{KEC},i+1/2} = \begin{pmatrix} \bar{\rho}\,\bar{\mathcal{X}}\,\bar{u}' \\ \bar{\rho}\,\bar{\mathcal{Z}}\,\bar{u}' \\ \bar{\rho}\,\bar{\mathcal{C}}\,\bar{u}' \\ \bar{\rho}\bar{u}'\boldsymbol{u} + \bar{p}\,\hat{\boldsymbol{n}} \\ \bar{\rho}\bar{u}'(\bar{e} + \bar{k}) + \bar{p}\bar{u}' \\ \bar{\rho}\bar{\nu}_t\bar{u}' \end{pmatrix} \tag{24}$$

Here, the bars indicate an average between the left and right data, as in $\bar{\rho} = (1/2)(\rho^L + \rho^R)$. For the kinetic energy, we use

$$\bar{k} = \frac{1}{2}(u^L u^R + v^L v^R + w^L w^R) \tag{25}$$

For second order, the nearest data are used: for example, $\bar{\rho}_{i+1/2} = (1/2)(\rho_i + \rho_{i+1})$; for a fourth- or higher-order flux formulation, gradients may be used to obtain a more accurate representation of the face variables. For the fourth-order flux used in this work, the left and right states are obtained using, for example,

$$u^L_{i+1/2} = u_i + \beta\nabla u_i\cdot(\boldsymbol{x}_{i+1/2} - \boldsymbol{x}_i) \tag{26a}$$

$$u^R_{i+1/2} = u_{i+1} + \beta\nabla u_{i+1}\cdot(\boldsymbol{x}_{i+1/2} - \boldsymbol{x}_{i+1}) \tag{26b}$$

with $\beta = 2/3$. As with the upwind-biased flux, we construct $\bar{e}$ from the face values of pressure, gas constant, and mass fractions.

C. Time Integration

The results presented in the following are based on a grid that resolves the boundary layer, because the RANS wall model is not valid unless the grid has a near-wall spacing corresponding to $y^+ \le 1$. For explicit time-integration methods, this approach imposes a stringent time-step limitation. Also, the source term on the reaction product equation may be large, imposing an additional time-step restriction on explicit methods. Therefore, implicit time-integration methods are used in the present work. For RANS simulations, the data-parallel line-relaxation method [45] is used, and for the wall-modeled LES, a second-order-accurate version of an implicit point-relaxation method [46] is employed; see also the work of Candler et al. [27,39]. As stated previously, the derivatives of the evolution-variable source term ζ are tabulated and used to form the Jacobian of the source term for use in the implicit operator.

VI. Test Cases

The EVM approach was used to simulate the normal injection of hydrogen in supersonic crossflow experiments of Gamba and Mungal [6] at two jet momentum flux J conditions. See the work of Saghafian et al. [18] for corresponding compressible flamelet-progress variable simulations. The EVM code was run in RANS mode (using second-order-accurate upwind fluxes, the Spalart–Allmaras model [35], and a large time step) and in wall-modeled LES mode as described in Sec. IV.

The computational domain was chosen to resolve the boundary layer on the flat plate; the injection plenum was gridded, and embedded refinement regions were included near the jet, in the jet interaction region, and in the jet plume. The near-wall grid was clustered to resolve the boundary layer, with the near-wall spacing corresponding to $y^+ \simeq 1$. Figure 3 shows the computational domain, along with a mixture fraction isosurface to visualize the jet plume. Figure 4 shows two images of the small grid, illustrating the embedded refinement regions. Note that the grid uses three-point and five-point singularities (where grid blocks join with either three or five edges at the block

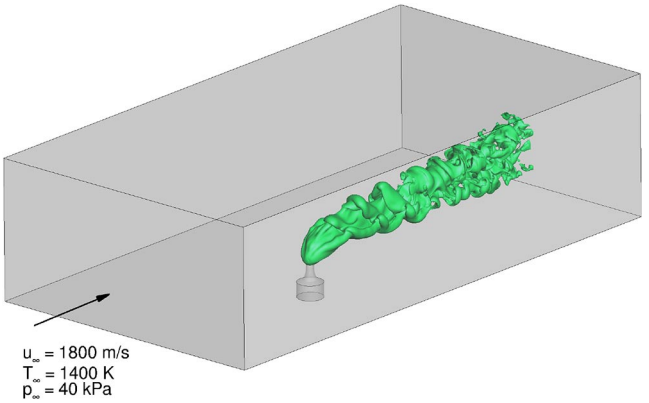

Fig. 3 Isosurface of mixture fraction ($\mathcal{Z} = 0.4$) to visualize the flowfield and solution domain.

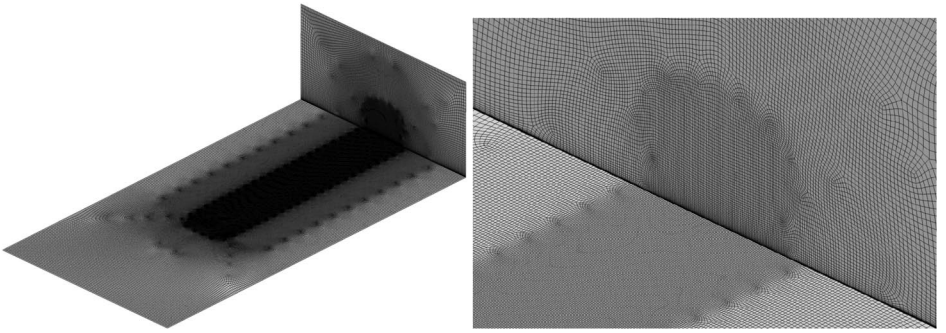

Fig. 4 Computational grid used for the simulations; surface grid on flat plate and outflow plane injector (left) and near outflow (right).

boundary) that allow the grid resolution to smoothly diminish away from the jet and plume. The grid was generated using the GoHypersonic Inc., LINK3D software [47]. There are a total of 14.1 million hexahedral elements in the grid shown. This grid was refined by approximately a factor of two in each direction, resulting in a finer grid with 107.4 million hexahedral elements.

The flow conditions are taken from the work of Gamba and Mungal [6] as $T_\infty = 1400$ K, $p_\infty = 40$ kPa, and $u_\infty = 1800$ m/s. This corresponds to a freestream density of 0.0995 kg/m^3, a Mach number of 2.48, and a Reynolds number of 6550 based on the 2 mm jet diameter and freestream conditions. The hydrogen plenum stagnation pressure and temperature were set to 1.098 MPa and 300 K for the jet momentum ratio case of $J = 2.7$, and to 2.034 MPa and 300 K for the $J = 5.0$ case. An isothermal surface temperature boundary condition at 300 K was assumed to represent the short-duration shock tube operation of the experiment.

For hydrogen–air combustion, we choose $\mathcal{C}$, which is the product fraction, to be the mass fraction of water: $\mathcal{C} = Y_{H_2O}$. The fuel mixture fraction $\mathcal{Z}$ is taken to be the total elemental mass fraction of hydrogen. The possible range of thermodynamic conditions in the experimental

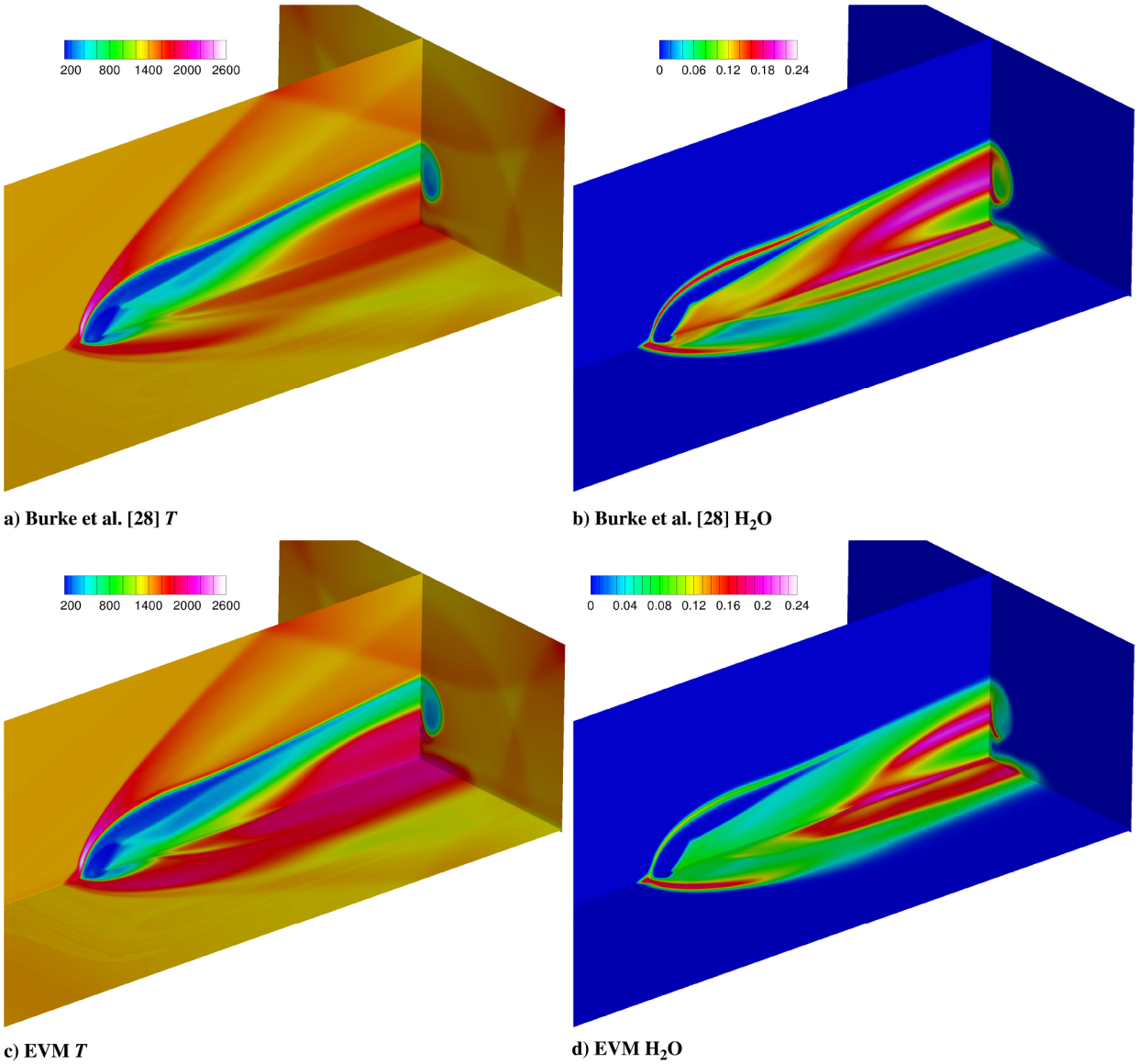

a) Burke et al. [28] T **b) Burke et al. [28] H_2O**

c) EVM T **d) EVM H_2O**

Fig. 5 Results of the $J = 5.0$ RANS on the 14.1-million-element grid: Burke et al. [28] model (top) and EVM (bottom) temperature (left, in K); and H_2O mass fraction (right).

flowfield is very large, particularly because the high-pressure hydrogen fuel overexpands to a Mach number of about 5.7. This results in a range of pressure between about 950 Pa and 2.47 MPa, and a range of temperatures between 48 and 2850 K. To cover this range of conditions, the EVM table was constructed for values of density between 0.001 and 2.651 $\mathrm{kg/m^3}$ and energies between −4.01 and 9.61 MJ/kg (referenced to $T = 298.15$ K). To better represent the variation of the gas state with the mixture fraction, the table was generated using the molar mixture fraction; the mass-based mixture fraction $\mathcal{Z}$ was then interpolated to its molar value. Nonuniform spacing in e and ρ was used to best represent the table for the bulk of the flowfield in which reactions were occurring. Coarse spacing in e and ρ was used where little reaction occurred (see Fig. 1). The EVM table used for the following simulations discretized e into 64 segments, ρ into 37, $\mathcal{Z}$ into 50, and τ into 58. We monitored the simulations and flagged conditions outside of the table; we then extended the table as needed. Ultimately, it would be useful modify the code so that it automatically generates new regions of the table during the LES calculation.

A. 14.1 Million Element Simulations-Element Grid Simulations

First, consider the simulations performed on the 14.1-million-element grid. Here, it is feasible to run simulations with the detailed chemical kinetics hydrogen–air model, allowing comparisons with the EVM approach. These comparisons are useful to show that the EVM approach produces results that are similar but not identical to the full kinetics model. This is expected because the models used in each approach are different and the variations indicate the sensitivity of the flowfield to the models used. Also, the development of the numerical method required a reference solution to understand the implications of the diffusive enthalpy flux modeling and several choices in the numerical flux function. We present results for the jet momentum ratio of $J = 5.0$; simulations were also run at $J = 2.7$, but the results were not appreciably different.

First, consider RANS simulations using the 11-species 23-reaction kinetics model of Burke et al. [28] and with the EVM approach run in RANS mode. The one-equation Spalart–Allmaras turbulence model [35] with the Catris–Aupoix [34] compressibility correction was used, and large time steps were used to rapidly converge the simulations to statistical steady state. Figure 5 plots the temperature and water mass-fraction fields for the RANS simulations on the domain centerline, at the exit plane, and slightly above the flat-plate surface. Note that these results are almost identical, with the same plume structure, extent of jet penetration, and levels of chemical reaction. The primary differences between the simulation occur in the reduced level of H_2O formation at the leading edge of the plume (the maximum values are 0.148 for the detailed model and 0.131 for EVM) and larger differences in the level of reaction under the jet plume just downstream of the jet

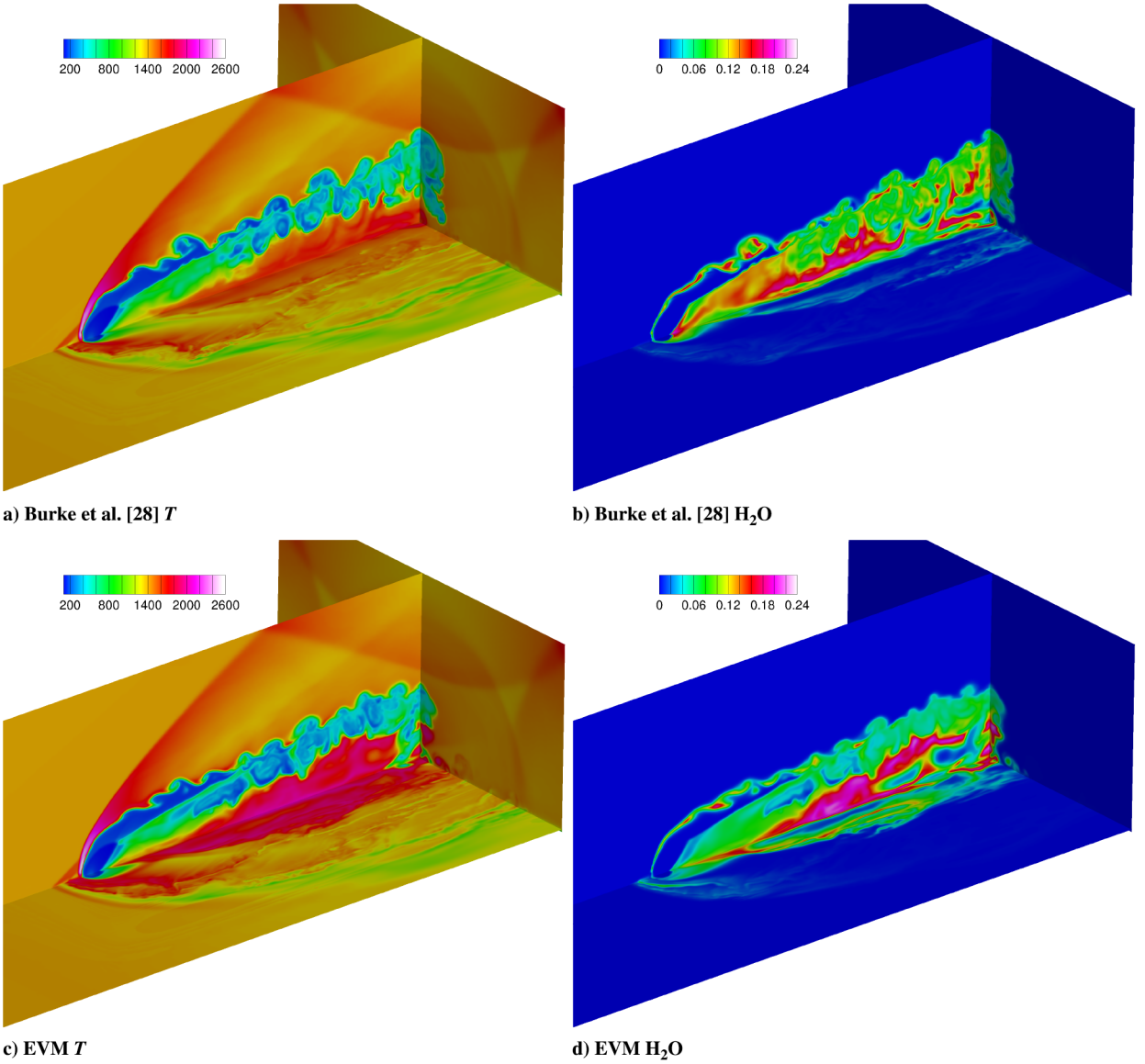

a) Burke et al. [28] T **b) Burke et al. [28] H_2O**

c) EVM T **d) EVM H_2O**

Fig. 6 Results of the $J = 5.0$ wall-modeled LES on the 14.1-million-element grid: Burke [28] model (top) and EVM (bottom): temperature (left, in K); and H_2O mass fraction (right).

orifice (here, EVM produces about half the H_2O as the full model). It should be noted that the EVM approach is designed for LES and is not necessarily expected to exactly match the RANS results; thus, this comparison is qualitative.

Corresponding simulations were run with wall-modeled LES using the improved delayed detached eddy simulation method of Shur et al. [37] and the fourth-order-accurate kinetic energy consistent low-dissipation fluxes. IDDES in combination with low-dissipation fluxes has been shown to compare well with jet in supersonic crossflow mixing experiments [48]. These cases were run with a second-order-accurate implicit time-integration method with a small time step, corresponding to a nondimensional time step with a Courant–Friedrichs–Lewy number of 20 and a physical time step of 7.0 ns. The simulations were initialized with the RANS flowfields,

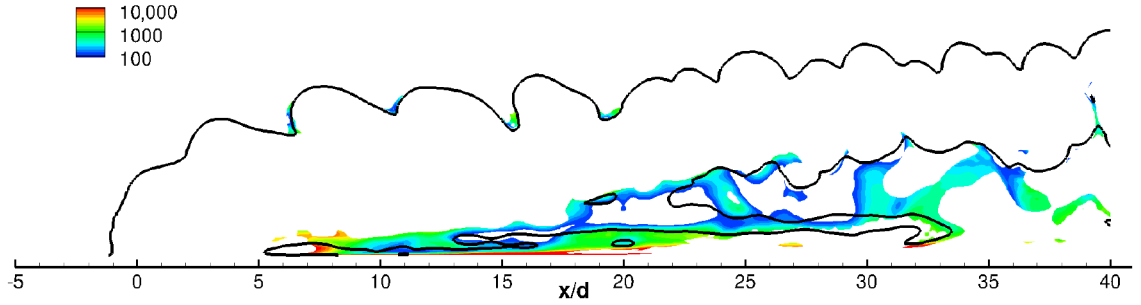

Fig. 7 Estimated Karlovitz number [Eq. (27)] on the centerline plane of the 14.1-million-element grid wall-modeled LES–EVM. The black line indicates $\phi = 1$.

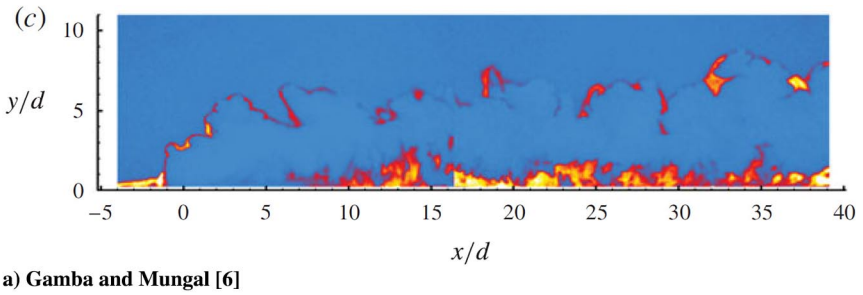

a) Gamba and Mungal [6]

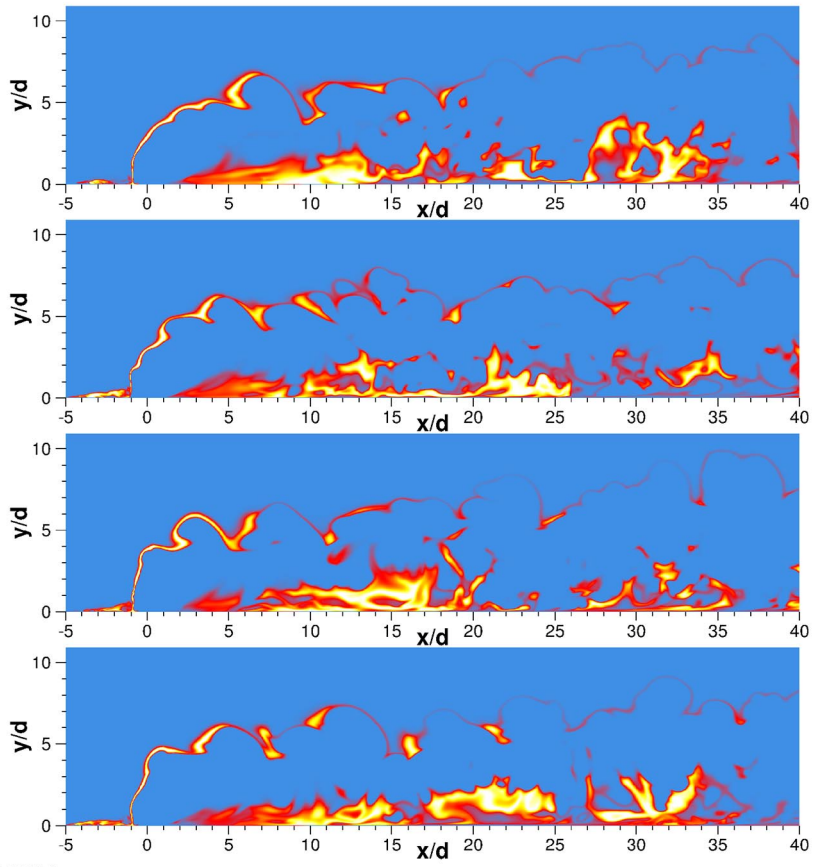

b) EVM

Fig. 8 Centerline OH-PLIF images from the Gamba and Mungal [6] experiment (top) and four images of the 107-million-element wall-modeled LES–EVM separated by 50 μs in time.

and they were run for at least 10 domain flowthrough times (the length of the domain divided by the freestream speed). The detailed kinetics simulations do not include an SGS model for the effective chemical reaction rate.

Figure 6 plots instantaneous snapshots of the temperature and H_2O mass fraction for these simulations. Note that the flowfields are highly unsteady, with intermittent temperature and product mass-fraction fields, which are characteristic of jets in supersonic crossflow. The detailed kinetics model and EVM approach yield similar results, with strong similarities in the overall plume structure and temperature fields. The dominant length scales of the unsteadiness are reproduced by the EVM approach. Note that the EVM has a reduced level of reaction in the region just downstream of the jet orifice, as seen in the RANS results (again differing by about a factor of two). Otherwise, the two simulations produce similar levels of reaction under the primary jet plume where near-wall burning dominates [6]. There is significant variation in the temperature fields due to unsteadiness; no attempt has been made to select pairs of images that give the best visual agreement. This variation will be addressed in more detail relative to the experimental data.

B. A Posteriori Analysis of Combustion Regime

In premixed combustion, the Karlovitz number Ka characterizes the reaction-zone length scale δ_R relative to the length scale of the dissipative turbulent eddies (Kolmogorov scale η_k) as

$$Ka = \left(\frac{\delta_R}{\eta_k}\right)^2, \quad \eta_k = \left(\frac{\nu^3}{\varepsilon}\right) \tag{27}$$

where ε is the turbulent dissipation rate, and ν is the molecular kinematic viscosity. We estimate $\varepsilon \simeq \nu_t \Omega^2$, with Ω as the magnitude of the vorticity; this is obtained from the definition of the eddy viscosity of $\nu_t = C_\mu k^2/\varepsilon$ and the form of the eddy viscosity used in the Spalart–Allmaras model [35] of $k = \hat{S}\nu_t/\sqrt{C_\mu}$, with $\hat{S} \simeq \Omega$ and k as the turbulent kinetic energy. The reaction-zone thickness is estimated from the work of Glassman et al. [49] as

$$\delta_R = \frac{\alpha}{S_L}, \quad S_L = \sqrt{\frac{\alpha \dot{\omega}_\mathcal{C}}{\beta \rho_u}} \tag{28}$$

where α is the unburned gas thermal diffusivity, S_L is the laminar flame speed, and β is the Zeldovich number (taken as $\beta = 10$). As Karlovitz number Ka increases, the turbulent eddies penetrate further through the reaction zone and more aggressively distort the flame or reaction zone [3].

Zhou et al. [5] showed experimentally that, for $Ka > 100$, combustion occurred in the DRZ regime. Figure 7 plots the estimated value of the Karlovitz number on the centerline of the wall-modeled LES using the EVM approach. Here, we have blanked regions where the gradient of $\mathcal{Z}$ is large (in regions of non-premixed combustion such as at the leading edge of the jet) and where the equivalence ratio ϕ is less than 0.5 or greater than two (where the fuel and air are not mixed). We also do not plot regions where the heat release is less than 4% of the maximum heat release, similar to Poturri and Edwards [50]. The plotted region of the Karlovitz number shows that there is a significant fraction of the flowfield where $Ka > 100$, indicating that combustion in those regions occurs in the DRZ regime. This is where the counter-rotating vortex pair causes intense turbulent motion, mixing the jet and freestream gases [48]. Gamba and Mungal [6] identified this region as dominated by distributed near-wall burning, and the present analysis shows that the large levels of turbulence produce distributed reactions.

These comparisons show that the EVM approach produces results that are consistent with the detailed kinetics model and that the EVM can represent combustion in the DRZ regime. The results of the compressible FPV results of Saghafian et al. [18] are notably different in the DRZ regime identified in the Karlovitz number analysis, with less near-wall burning where $Ka > 100$ in Fig. 7.

C. Computational Cost

The computational costs of the two simulation approaches are significantly different. The 11-species detailed kinetics model requires 3.98 times more computational time than the EVM approach. The cost of the implicit numerical method used in this work has been shown to scale quadratically with the number of equations being solved [51]. For the detailed model, there are 11 species equations, three momentum equations, an energy equation, and a turbulence equation: for a total of 16. With EVM, there are three mass conservation equations ($\rho\mathcal{X}$, $\rho\mathcal{Z}$, and $\rho\mathcal{C}$), along with the other equations, for a total of eight. Thus, this simple scaling indicates that the EVM should be about $(16/8)^2 = 4$ times faster than the detailed model; thus, the measured computational time is consistent with the expected scaling. Therefore, the cost of computing thermodynamic quantities that depend on the total number of species in the detailed model is not significant for this case. For more complex kinetics models, the EVM approach will be correspondingly more efficient. Furthermore, the present numerical method has the same numerical stability properties as the well-established detailed simulation approach [27].

D. 107-Million-Element Grid Simulations

The $J = 5.0$ case was run on the 107-million-element grid and compared with the hydroxyl radical planar laser-induced fluorescence (OH-PLIF) measurements of Gamba and Mungal [6]. The OH-PLIF signal was computed from the computational simulation data using the computer code provided by Gamba and based on his Ph.D. thesis [52]. Figure 8 plots the experimental OH-PLIF signal (top) with EVM simulation results taken at four different times separated by 50 μs (corresponding to a flow distance of 45 injector diameters at the inflow speed). The experiments were

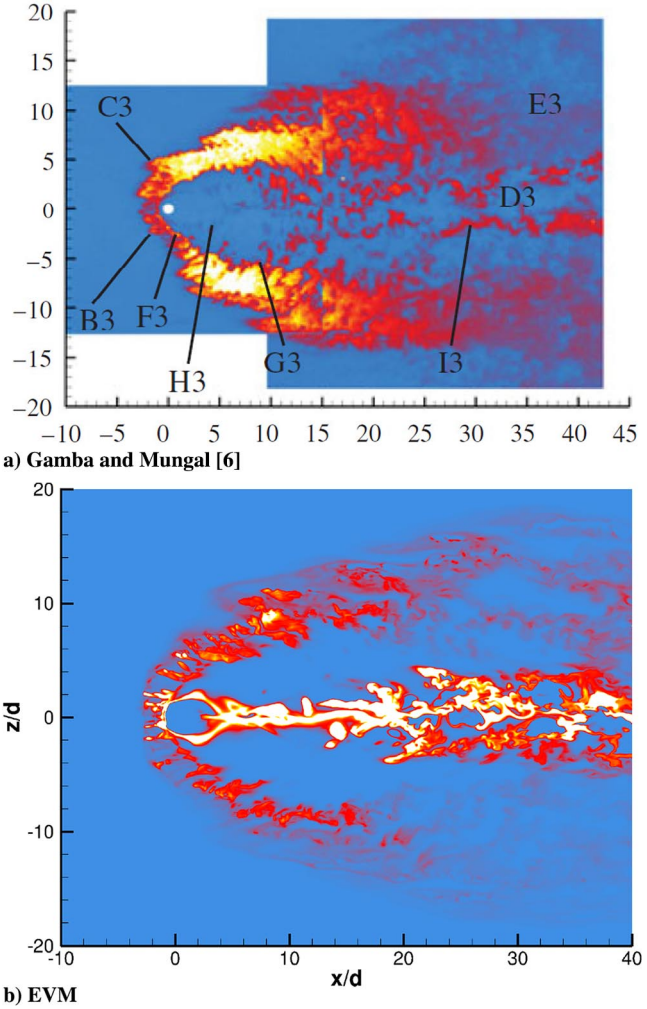

a) Gamba and Mungal [6]

b) EVM

Fig. 9 OH-PLIF images on a plane located at $y/d = 0.5$ above the flat plate from the Gamba and Mungal [6] experiment (top) and the 107-million-element wall-modeled LES–EVM (bottom).

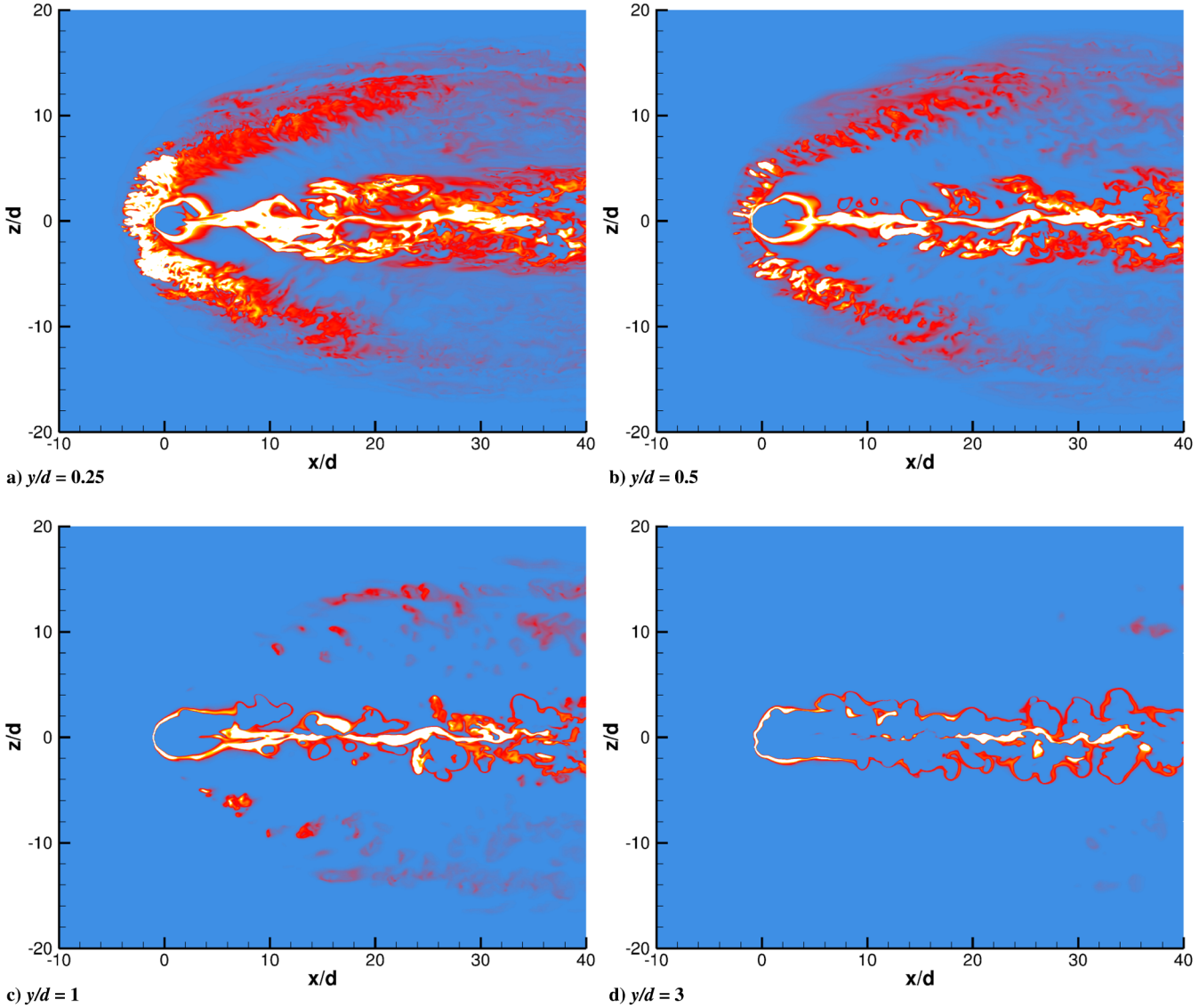

Fig. 10 OH-PLIF images on planes parallel to the flat plate from the 107-million-element wall-modeled LES–EVM.

not calibrated to obtain quantitative OH-PLIF signals; thus, it is not possible to quantitatively compare the OH-PLIF signal level from the experiments with the simulations, and thus the comparisons are qualitative. The present figures were made to best match the color map and maximum signal levels used by Gamba and Mungal [6]; all simulation data were plotted with the same color map.

Note the close agreement between the experiment and the EVM simulations. Both have three main reaction zones: an intermittent flame front at the upper edge of the jet, a DRZ in the near-wall region under the jet, and a DRZ in the boundary layer surrounding the injector. The EVM simulations correctly capture the jet penetration and the approximate length scale of the variations in the flame front. Both show regions of near extinction and more aggressive reaction. In the complex lifted region under the jet plume, the experiments show clear evidence of intermittent near-wall burning, which is characteristic of combustion in the DRZ regime. The EVM simulations also produce this combustion behavior, with large variations in the extent of near-wall burning, as seen by comparing the simulation snapshots. Again, the EVM simulations are consistent with the experimental data, given the inherent temporal variation. See the work of Saghafian et al. [18] for a corresponding image obtained with a compressible flamelet progress variable approach.

Figure 9 plots the OH-PLIF experimental and EVM simulation data in a plane located at $y/d = 0.5$ above the flat plate. Again, we have attempted to match the color map between the two images. The horseshoe vortex that wraps around the jet is readily apparent, and the combustion that occurs in this region is visualized by the OH-PLIF signal. Generally, the EVM simulation predicts the extent and variation of the OH-PLIF signal very well, but there is significantly more hydroxyl radical (OH) close to the jet and on the centerline ($z/d = 0$). It appears that the excess OH originates in the vortices that wrap around the jet and are swept into the centerline flow. The EVM simulation relies on a RANS-based wall model that suppresses unsteadiness and does not permit small-scale motion; thus, it is not surprising that the wall-modeled LES does not correctly predict this near-wall behavior.

Figure 10 shows additional visualizations of the computed OH-PLIF in four wall-parallel planes; in comparison to the images of Gamba and Mungal [6], these images further illustrate the good overall agreement between the EVM and the experiment.

VII. Conclusions

The evolution-variable manifold approach of Cymbalist and Dimotakis [25,26] has been implemented in a parallel implicit unstructured grid CFD code and compared with an experimental test case of reacting hydrogen in a supersonic crossflow. The EVM approach precomputes and tabulates the chemical composition and rate of change of the evolution variable as a function of the computed density, energy, mixture fraction, and evolution variable. The thermodynamic state and transport properties are then computed directly from the composition. Within the EVM framework, a thermodynamically consistent numerical flux function was formulated for both dissipative upwind-biased fluxes and low-

dissipation high-order centered fluxes. The coupling between the EVM tabulated data and the numerical simulations was described.

Results for the hydrogen-injection experiments of Gamba and Mungal [6] were obtained with the EVM method on a 14.1-million-element grid, run in both RANS and wall-modeled LES modes. Corresponding simulations using the full 11-species chemical kinetics model of Burke et al. [28] were also performed. The EVM simulations are found to be in good agreement with the full kinetics model for both sets of simulations. The overall plume structure, jet penetration, temperature distribution, and product formation are consistent between the two approaches. The EVM approach captures both the thin reaction zones at the edge of the jet and the distributed reaction zones underneath the jet plume. The wall-modeled LES results obtained with the detailed model and the EVM are strikingly similar to one another and produce similar jet length scales, temperature variations, and water formation. The EVM approach requires approximately one-fourth the computer time as the detailed kinetics model, and it has the same numerical stability properties as the well-established implicit method. The ratio of the computational cost would increase for simulations involving more complex fuels and the transport and reaction of a larger number of species.

Simulations were run on a larger grid (107 million elements) to compare with the experimental measurements of OH planar laser-induced fluorescence of Gamba and Mungal [6]. These comparisons clearly illustrate that the EVM approach captures the thin reaction fronts and the distributed reaction zones that dominate this flow. In particular, the intermittent near-wall burning observed in the experiments is well represented by the EVM approach. The simulations produce excess OH signal in the near-wall region just downstream of the jet orifice; this is likely due to the suppression of the unsteadiness by the RANS-based wall model used here.

The evolution-variable manifold approach shows promise for the simulation of high-speed flows that are dominated by autoignition effects and combustion in the distributed reaction-zone regime. The simulations illustrate that the approach may be implemented in a production CFD code and used to analyze realistic configurations. Work continues to compare the EVM model with more established turbulent combustion modeling approaches and to simulate more complex hydrocarbon combustion flows.

Appendix A: ζ Dependence on χ

The dependence of the source term ζ on the forcing term χ depends on the thermodynamic state. Generally, χ has a larger effect at conditions favoring slower chemical reactions, and particularly at lower densities; whereas it has negligible effects where reaction rates are large. Figure A1 plots the value of ζ for hydrogen–air as a function of τ for rich ($\mathcal{Z} > \mathcal{Z}_{st}$), lean ($\mathcal{Z} < \mathcal{Z}_{st}$), and stoichiometric conditions ($\mathcal{Z} = \mathcal{Z}_{st}$), where $\mathcal{Z}_{st} = 0.0284$ is the stoichiometric mass-based mixture fraction, for several values of χ ranging between 10^3 and 10^4 s^{-1}. The fuel–air equivalence ratio is ϕ. The top row of plots shows the results for high-density cases ($\rho = 1$ kg/m^3), and the bottom row shows the results for low-density cases ($\rho = 0.1$ kg/m^3). The internal energy is 0 J/kg for all cases (with a reference temperature of 298.15 K).

At high density with large chemical reaction rates ($\zeta_{max} \sim 5 \times 10^5$ s^{-1} for $\phi = 1$), the $\zeta(\tau)$ plots overlap for all values of χ and all values of ϕ, confirming that the effects of χ on ζ can be neglected where combustion is robust. At lower densities where chemical reaction rates are much lower ($\zeta_{max} \sim 5 \times 10^4$ s^{-1} for $\phi = 1$), $\zeta(\tau)$ for $\chi = 10^4$ is approximately 20% larger than $\zeta(\tau)$ for $\chi = 10^3$, for all values of ϕ.

These results are consistent with the intended purpose of χ, which is to provide a parameter that models (to zeroth order) SGS processes that promote fluid evolution toward thermochemical equilibrium, especially at conditions where the evolution toward equilibrium is slow (e.g., low density).

Appendix B: Path Independence

In the EVM framework, it is assumed that the state of the Lagrangian WSR does not depend on its trajectory through $[e, \rho, \mathcal{Z}]$ space when tabulated versus τ. This reaction trajectory independence allows straight-line trajectories to be used to generate the EVM

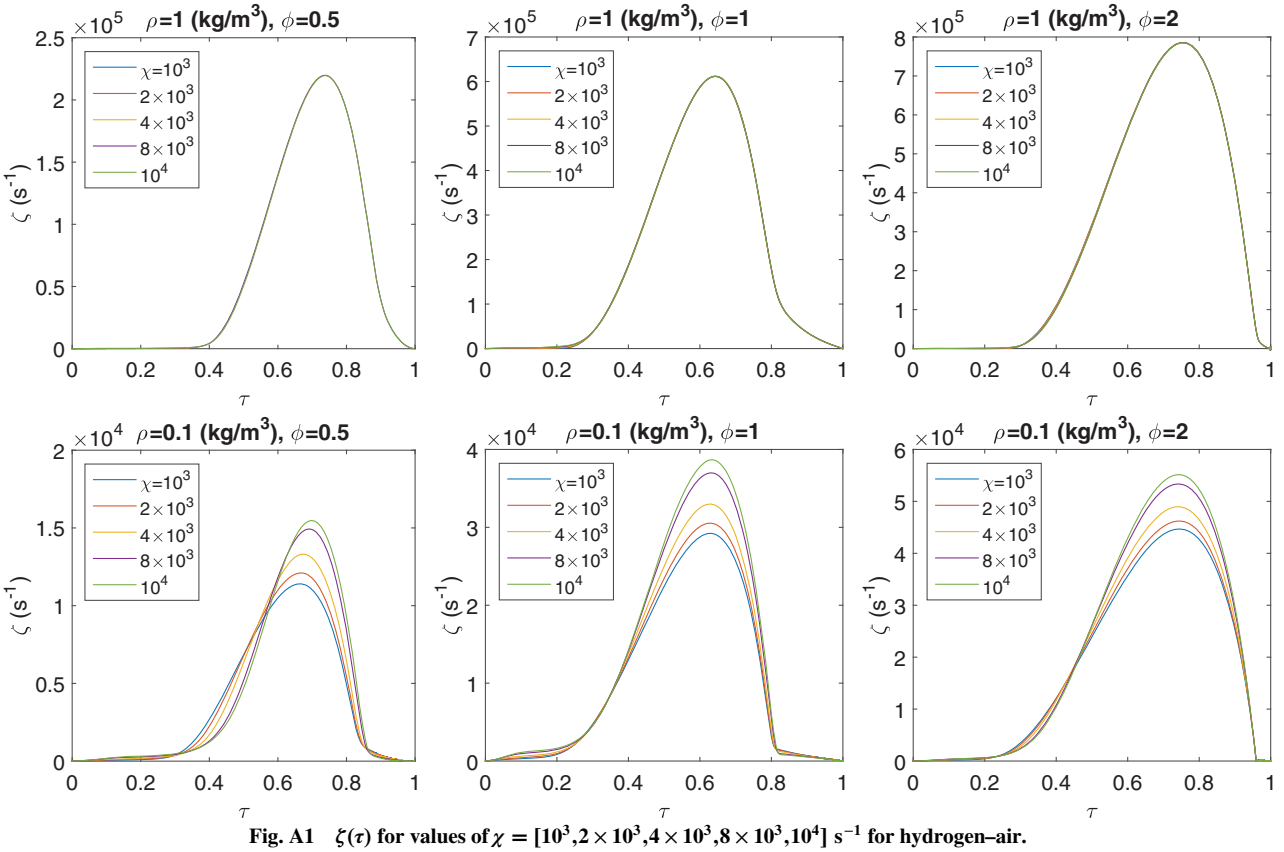

Fig. A1 $\zeta(\tau)$ for values of $\chi = [10^3, 2\times10^3, 4\times10^3, 8\times10^3, 10^4]$ s^{-1} for hydrogen–air.

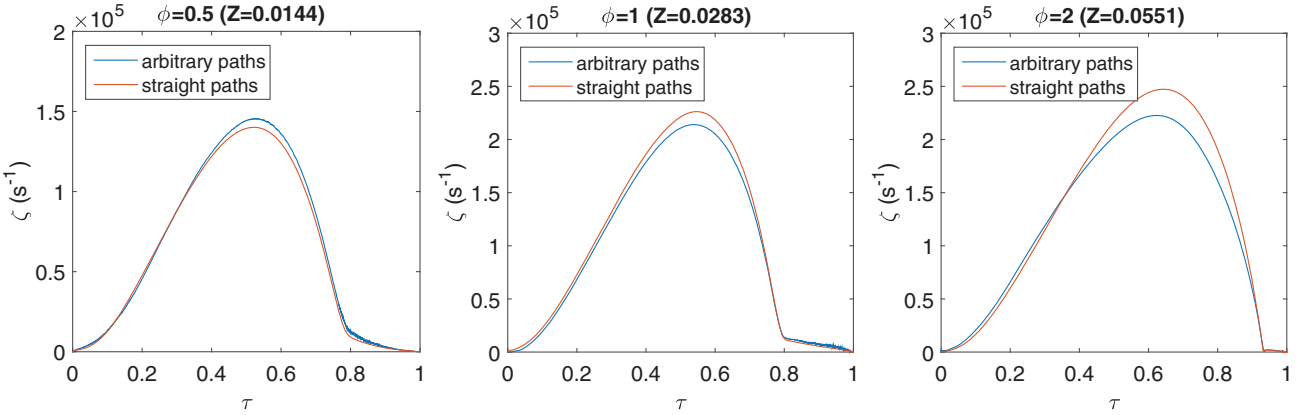

Fig. B1 Value of ζ as a function of τ in tables computed using straight and arbitrary (nonstraight) trajectories.

tables; a straight-line trajectory is defined as a WSR that has a constant value of $[e, \rho, \mathcal{Z}]$ as it evolves from an unburned ($\tau = 0$) to a burned ($\tau = 1$) state. It must be verified that the assumption that a straight-line trajectory adequately represents an arbitrary trajectory through $[e, \rho, \mathcal{Z}]$-space.

The extent of trajectory independence can be demonstrated by comparing fluid properties (composition and reaction rates, in particular) at a point in $[e, \rho, \mathcal{Z}, \tau]$ space for fluid elements that have reached that state on different (nonstraight) paths. Equivalently, arbitrary nonstraight paths can be used to populate a sample table that can then be compared to a corresponding table generated with straight-line trajectories. Differences between the two tables can be used to quantify the validity of the straight-line reaction trajectory assumption. Additionally, differences between the two tables can be incorporated into a quantitative uncertainty estimate of the LES results. The latter approach is taken here.

Two tables with ranges of $0.5 \leq e(\mathrm{MJ/kg}) \leq 1, 0.15 \leq \rho(\mathrm{kg/m^3}) \leq 0.3$, and $0.01 \leq \mathcal{Z} \leq 0.06$ were constructed for hydrogen–air with arbitrary nonstraight-line reaction trajectories and with straight-line reaction trajectories. The equations used to generate arbitrary trajectories were an extension of the WSR equations [Eq. (1)]:

$$\frac{\mathrm{d}Y_s}{\mathrm{d}t} = \chi(Y_{s,\mathrm{eq}} - Y_s) + \dot{\omega}_s \tag{B1a}$$

$$\frac{\mathrm{d}e}{\mathrm{d}t} = \chi(e_{\mathrm{eq}} - e) \tag{B1b}$$

$$\frac{\mathrm{d}\rho}{\mathrm{d}t} = \chi(\rho_{\mathrm{eq}} - \rho) \tag{B1c}$$

where $[e_{\mathrm{eq}}, \rho_{\mathrm{eq}}, \mathcal{Z}_{\mathrm{eq}}]$ are randomly selected from the relevant table range, and are held constant on each arbitrary trajectory. $Y_{s,\mathrm{eq}}$ is the equilibrium mass-fraction vector at $[e_{\mathrm{eq}}, \rho_{\mathrm{eq}}, \mathcal{Z}_{\mathrm{eq}}]$. The resulting trajectories are not straight, in the sense that $[e, \rho, \mathcal{Z}]$ varies with τ. This approach provides a random perturbation to each WSR as it evolves from $\tau = 0$ to $\tau = 1$. Twenty-thousand trajectories were computed and used to populate the first table by averaging (at reaction trajectory intersection points) and interpolating the results onto a uniform grid. The second straight-line table was constructed as discussed in the main text, by keeping $[e, \rho, \mathcal{Z}]$ constant.

Figure B1 plots ζ as a function of τ from the tables computed using straight and arbitrary (nonstraight) paths for lean ($\phi = 0.5$, left), stoichiometric ($\phi = 1$, center), and rich ($\phi = 2$, right) conditions. The results show that, at stoichiometric and lean conditions, the tables are very similar, and the assumption of path independence is valid. At rich conditions, the reaction rates differ by up to 10% of the maximum value, indicating that the assumption of trajectory independence at fuel-rich conditions propagates uncertainty on the order of 10% into the LES results.

Acknowledgments

This work was sponsored by the U.S. Air Force Office of Scientific Research (AFOSR) Grant FA9550-12-1-0461. We would like to thank Mirko Gamba for providing the code to compute the hydroxyl radical planar laser-induced fluorescence images. The views and conclusions contained herein are those of the authors and should not be interpreted as necessarily representing the official policies or endorsements, either expressed or implied, of the AFOSR or the U.S. Government.

References

[1] Borghi, R., "Mise au Point sur la Structure des Flammes Turbulentes," *Journal de Chimie Physique*, Vol. 81, No. 6, 1984, pp. 361–370.

[2] Peters, N., "Laminar Flamelet Concepts in Turbulent Combustion," *Proceedings of the Symposium (International) on Combustion*, Vol. 21, No. 1, 1988, pp. 1231–1250. doi:10.1016/S0082-0784(88)80355-2

[3] Law, C. K., *Combustion Physics*, Cambridge Univ. Press, New York, 2006, p. 499.

[4] Aspden, A. J., Day, M. S., and Bell, J. B., "Turbulence–Flame Interactions in Lean Premixed Hydrogen: Transition to the Distributed Burning Regime," *Journal of Fluid Mechanics*, Vol. 680, 2011, pp. 287–320. doi:10.1017/jfm.2011.164

[5] Zhou, B., Brackmann, C., Li, Z., Alden, M., and Bai, X.-S., "Simultaneous Multi-Species and Temperature Visualization of Premixed Flames in the Distributed Reaction Zone Regime," *Proceedings of the Combustion Institute*, Vol. 35, No. 2, 2015, pp. 1409–1416. doi:10.1016/j.proci.2014.06.107

[6] Gamba, M., and Mungal, M. G., "Ignition, Flame Structure and Near-Wall Burning in Transverse Hydrogen Jets in Supersonic Crossflow," *Journal of Fluid Mechanics*, Vol. 780, Oct. 2015, pp. 226–273. doi:10.1017/jfm.2015.454

[7] Fureby, C., "LES for Supersonic Combustion," AIAA Paper 2012-5979, Sept. 2012.

[8] Foster, J. W., and Miller, R. S., "Survey of Turbulent Combustion Models for Large Eddy Simulations of Propulsive Flowfields," AIAA Paper 2015-1379, Jan. 2015.

[9] Oefelein, J. C., "Analysis of Turbulent Combustion Modeling Approaches for Aero-Propulsive Applications," AIAA Paper 2015-1378, Jan. 2015.

[10] Gonzalez-Juez, E. D., Kerstein, A. R., Menon, S., and Ranjan, R., "An Analysis of the Basic Assumptions of Turbulent Combustion Models with Emphasis on High-Speed Flows," AIAA Paper 2015-1380, Jan. 2015.

[11] Pierce, C. D., and Moin, P., "Progress-Variable Approach for Large-Eddy Simulation of Non-Premixed Turbulent Combustion," *Journal of Fluid Mechanics*, Vol. 504, 2004, pp. 73–97. doi:10.1017/S0022112004008213

[12] Fiorina, B., Veynante, D., and Candel, S., "Modeling Combustion Chemistry in Large Eddy Simulation of Turbulent Flames," *Flow, Turbulence and Combustion*, Vol. 94, No. 1, 2015, pp. 3–42. doi:10.1007/s10494-014-9579-8

[13] Menon, S., and Kerstein, A. R., "The Linear-Eddy Model," *Turbulent Combustion Modeling*, Springer, Dordrecht, The Netherlands, 2011, pp. 221–247.
[14] Hiremath, V., Ren, Z., and Pope, S. B., "Combined Dimension Reduction and Tabulation Strategy Using ISAT-RCCE-GALI for the Efficient Implementation of Combustion Chemistry," *Combustion and Flame*, Vol. 158, No. 11, 2011, pp. 2113–2127. doi:10.1016/j.combustflame.2011.04.010
[15] Pope, S. B., "PDF Methods for Turbulent Reactive Flows," *Progress in Energy and Combustion Science*, Vol. 11, No. 2, 1985, pp. 119–192. doi:10.1016/0360-1285(85)90002-4
[16] Colucci, P. J., Jaberi, F. A., Givi, P., and Pope, S. B., "Filtered Density Function for Large Eddy Simulation of Turbulent Reacting Flows," *Physics of Fluids*, Vol. 10, No. 2, 1998, pp. 499–515. doi:10.1063/1.869537
[17] Chan, W. L., and Ihme, M., "Large-Eddy Simulations of a Dual-Mode Scramjet Combustor: Operating Point A of University of Virginias Scramjet Experiments," AIAA Paper 2014-1161, Jan. 2014.
[18] Saghafian, A., Terrapon, V. E., and Pitsch, H., "An Efficient Flamelet-Based Combustion Model for Compressible Flows," *Combustion and Flame*, Vol. 162, No. 3, March 2015, pp. 652–667. doi:10.1016/j.combustflame.2014.08.007
[19] Wang, H., Piao, Y., and Niu, J., "IDDES Simulation of Supersonic Combustion Using Flamelet Modeling," AIAA Paper 2015-3211, June 2015.
[20] Cao, C., Ye, T., and Zhao, M., "Large Eddy Simulation of Hydrogen/Air Scramjet Combustion Using Tabulated Thermo-Chemistry Approach," *Chinese Journal of Aeronautics*, Vol. 28, No. 5, 2015, pp. 1316–1327. doi:10.1016/j.cja.2015.08.008
[21] Génin, F., and Menon, S., "Simulation of Turbulent Mixing Behind a Strut in Supersonic Flow," *AIAA Journal*, Vol. 48, No. 3, 2010, pp. 526–539. doi:10.2514/1.43647
[22] Delarue, B. J., and Pope, S. B., "Calculations of Subsonic and Supersonic Turbulent Reacting Mixing Layers Using Probability Density Function Methods," *Physics of Fluids*, Vol. 10, No. 2, 1998, pp. 487–498. doi:10.1063/1.869536
[23] Cocks, P. A. T., Dawes, W. N., and Cant, R. S., "The Influence of Turbulence-Chemistry Interaction Modeling for Supersonic Combustion," AIAA Paper 2011-0306, Jan. 2011.
[24] Irannejad, A., Jaberi, F., Komperda, J., and Mashayek, F., "Large Eddy Simulation of Supersonic Turbulent Combustion with FMDF," AIAA Paper 2014-1188, Jan. 2014.
[25] Cymbalist, N., Mixing, Chemical Reactions, and Combustion in Supersonic Flows, Ph.D. Thesis, California Inst. of Technology, Pasadena, CA, June 2016.
[26] Cymbalist, N., and Dimotakis, P. E., "On Autoignition-Dominated Supersonic Combustion," AIAA Paper 2015-2315, June 2015.
[27] Candler, G. V., Johnson, H. B., Nompelis, I., Subbareddy, P. K., Gidzak, V., and Barnhardt, M. D., "Development of the US3D Code for Advanced Compressible and Reacting Flow Simulations," AIAA Paper 2015-1893, Jan. 2015.
[28] Burke, M. P., Chaos, M., Ju, Y., Dryer, F. L., and Klippenstein, S. J., "Comprehensive H_2/O_2 Kinetic Model for High-Pressure Combustion," *International Journal of Chemical Kinetics*, Vol. 44, No. 7, 2012, pp. 444–474. doi:10.1002/kin.v44.7
[29] Li, C., Kailasanath, K., and Oran, E. S., "Detonation Structures by Multiple Shocks on Ram-Accelerator Projectiles," *Combustion and Flame*, Vol. 108, Nos. 1–2, 1997, pp. 173–186. doi:10.1016/S0010-2180(96)00102-2
[30] Gao, Y., Shan, R., Lyra, S., Li, C., Wang, H., Chen, J. H., and Lu, T., "On Lumped-Reduced Reaction Model for Combustion of Liquid Fuels," *Combustion and Flame*, Vol. 163, 2016, pp. 437–446. doi:10.1016/j.combustflame.2015.10.018
[31] McBride, B. J., and Gordon, S., "Computer Program for Calculation of Complex Chemical Equilibrium Compositions and Applications," NASA Rept. RP-1311, June 1996.
[32] Oevermann, M., "Numerical Investigation of Turbulent Hydrogen Combustion in a SCRAMJET Using Flamelet Modeling," *Aerospace Science and Technology*, Vol. 4, No. 7, 2000, pp. 463–480. doi:10.1016/S1270-9638(00)01070-1
[33] Quinlan, J. R., Drozda, T. G., McDaniel, J. C., Lacaze, G., and Oefelein, J., "A Priori Analysis of a Compressible Flamelet Model using RANS Data for a Dual-Mode Scramjet Combustor," AIAA Paper 2015-3208, June 2015.
[34] Catris, S., and Aupoix, B., "Density Corrections for Turbulence Models," *Aerospace Science and Technology*, Vol. 4, No. 1, 2000, pp. 1–11. doi:10.1016/S1270-9638(00)00112-7
[35] Spalart, P. R., and Allmaras, S. R., "A One-Equation Turbulence Model for Aerodynamic Flows," AIAA Paper 1992-0439, Jan. 1992.
[36] Rumsey, C., Turbulence Modeling Resource [online database], NASA Langley Research Center, Hampton, VA, https://turbmodels.larc.nasa.gov [retrieved 15 Dec. 2016].
[37] Shur, M. L., Spalart, P. R., Strelets, M. K., and Travin, A. K., "A Hybrid RANS-LES Approach with Delayed-DES and Wall-Modelled LES Capabilities," *International Journal of Heat and Fluid Flow*, Vol. 29, No. 6, 2008, pp. 1638–1649. doi:10.1016/j.ijheatfluidflow.2008.07.001
[38] Smagorinsky, J., "General Circulation Experiments with the Primitive Equations," *Monthly Weather Review*, Vol. 91, No. 3, 1963, pp. 99–164. doi:10.1175/1520-0493(1963)091<0099:GCEWTP>2.3.CO;2
[39] Candler, G. V., Subbareddy, P. K., and Brock, J. M., "Advances in Computational Fluid Dynamics Methods for Hypersonic Flows," *Journal of Spacecraft and Rockets*, Vol. 52, No. 1, Jan.–Feb. 2015, pp. 17–28. doi:10.2514/1.A33023
[40] MacCormack, R. W., *Numerical Computation of Compressible and Viscous Flow*, AIAA Education Series, AIAA, Reston, VA, 2014, pp. 181–183.
[41] Roe, P., "Characteristic-Based Schemes for the Euler Equations," *Annual Review of Fluid Mechanics*, Vol. 18, No. 1, 1986, pp. 337–365. doi:10.1146/annurev.fl.18.010186.002005
[42] van Leer, B., "Towards the Ultimate Conservative Difference Scheme, V. A Second Order Sequel to Godunov's Method," *Journal of Computational Physics*, Vol. 32, No. 1, 1979, pp. 101–136. doi:10.1016/0021-9991(79)90145-1
[43] Subbareddy, P., and Candler, G. V., "A Fully-Discrete, Kinetic Energy Consistent Finite Volume Scheme for Compressible Flows," *Journal of Computational Physics*, Vol. 228, No. 5, March 2009, pp. 1347–1364. doi:10.1016/j.jcp.2008.10.026
[44] Ducros, F., Ferrand, V., Nicoud, F., Weber, C., Darracq, D., Gacherieu, C., and Poinsot, T., "Large-Eddy Simulation of Shock/Turbulence Interaction," *Journal of Computational Physics*, Vol. 152, No. 2, 1999, pp. 517–549. doi:10.1006/jcph.1999.6238
[45] Wright, M. J., Bose, D., and Candler, G. V., "A Data-Parallel Line Relaxation Method for the Navier–Stokes Equations," *AIAA Journal*, Vol. 36, No. 9, Sept. 1998, pp. 1603–1609. doi:10.2514/2.586
[46] Wright, M. J., Candler, G. V., and Prampolini, M., "Data Parallel Lower-Upper Relaxation Method for the Navier–Stokes Equations," *AIAA Journal*, Vol. 34, No. 7, July 1996, pp. 1371–1377. doi:10.2514/3.13242
[47] Drayna, T. W., Haag, C. J. W., Bartkowicz, M. D., and Gidzak, V. M., LINK3D, Software Package, Ver. 0.9.0, GoHypersonic, Inc., Minneapolis, MN, 2016.
[48] Peterson, D. M., and Candler, G. V., "Hybrid Reynolds-Averaged and Large-Eddy Simulation of Normal Injection into a Supersonic Crossflow," *Journal of Propulsion and Power*, Vol. 26, No. 3, 2010, pp. 533–544. doi:10.2514/1.46810
[49] Glassman, I., Yetter, R. A., and Glumac, N. G., *Combustion*, 5th ed., Elsevier, New York, 2015, pp. 153–158.
[50] Potturi, A. S., and Edwards, J. R., "Large-Eddy/Reynolds-Averaged Navier–Stokes Simulation of Cavity-Stabilized Ethylene Combustion," *Combustion and Flame*, Vol. 162, No. 4, 2015, pp. 1176–1192. doi:10.1016/j.combustflame.2014.10.011
[51] Candler, G. V., Subbareddy, P., and Nompelis, I., "A Decoupled Implicit Method for Aerothermodynamics and Reacting Flows," *AIAA Journal*, Vol. 51, No. 5, May 2013, pp. 1245–1254. doi:10.2514/1.J052070
[52] Gamba, M., "Volumetric PIV and OH PLIF Imaging in the Far Field of Nonpremixed Jet Flames," Ph.D. Thesis, Univ. of Texas at Austin, Austin, TX, 2009.

Y. Ju
Associate Editor